Miles D. Blanchet 0; Bethany E. Matthews 0; Steven R. Spurgeon 0; Steve M. Heald 0; Tamara Isaacs-Smith 0; Ryan B. Comes 0



Journal of Vacuum Science & Technology A 41, 052703 (2023)

https://doi.org/10.1116/6.0002329





CrossMark



Jahn-Teller-driven phase segregation in $Mn_xCo_{3-x}O_4$ spinel thin films

Cite as: J. Vac. Sci. Technol. A 41, 052703 (2023); doi: 10.1116/6.0002329

Submitted: 3 November 2022 · Accepted: 12 June 2023 ·

Published Online: 12 July 2023







Miles D. Blanchet, 1 D Bethany E. Matthews, 2 D Steven R. Spurgeon, 2.3 D Steve M. Heald, 4 D Tamara Isaacs-Smith, 1 🔟 and Ryan B. Comes 1,a) 🔟

AFFILIATIONS

- Department of Physics, Auburn University, Auburn, Alabama 36849
- ²Energy and Environment Directorate, Pacific Northwest National Laboratory, Richland, Washington 99354
- Department of Physics, University of Washington, Seattle, Washington 98195
- ⁴Advanced Photon Source, Argonne National Laboratory, Argonne, Illinois 60439

ABSTRACT

Transition metal spinel oxides comprised of earth-abundant Mn and Co have long been explored for their use in catalytic reactions and energy storage. However, understanding functional properties can be challenging due to differences in sample preparation and the ultimate structural properties of the materials. Epitaxial thin film synthesis provides a novel means of producing precisely controlled materials to $\frac{8}{5}$ explore the variations reported in the literature. In this work, $Mn_xCo_{3-x}O_4$ samples from x = 0 to x = 1.28 were synthesized through molecuexplore the variations reported in the literature. In this work, $Mn_xCo_{3-x}O_4$ samples from x = 0 to x = 1.28 were synthesized through molecular beam epitaxy and characterized to develop a material properties map as a function of stoichiometry. Films were characterized via *in situ* $\frac{8}{8}$ x-ray photoelectron spectroscopy, x-ray diffraction, scanning transmission electron microscopy, and polarized K-edge x-ray absorption spectroscopy. Mn cations within this range were found to be octahedrally coordinated, in line with an inverse spinel structure. Samples largely show mixed Mn³⁺ and Mn⁴⁺ character with evidence of phase segregation tendencies with the increasing Mn content and increasing Mn formal charge. Phase segregation may occur due to structural incompatibility between cubic and tetragonal crystal structures associated with Mn⁴⁺ and Jahn-Teller active Mn³⁺ octahedra, respectively. Our results help in explaining the reported differences across samples in these promising materials for renewable energy technologies.

Published under an exclusive license by the AVS. https://doi.org/10.1116/6.0002329

I. INTRODUCTION

Materials that exhibit oxygen reduction reactivity (ORR) are important for the development of catalytic technologies such as electrolyzers, metal-air batteries, and fuel cells.¹⁻⁷ While materials containing expensive elements such as platinum dominate current catalysis research, 1,3,8,9 cheaper alternatives such as transition metal oxide spinels containing manganese, cobalt, nickel, and iron have been shown to exhibit ORR levels on par with platinum-based materials. 1,10-12 This includes the spinels of the cobalt-manganese system, CoMn₂O₄ (CMO) and MnCo₂O₄ (MCO), 1,11,13-16 where previous work has demonstrated their impressive ORR properties. 17 While both CMO and MCO are relatively understudied in the literature, an investigation of CMO thin film material properties from ideal to Co-rich cation stoichiometry was recently published.²¹ The properties of MCO in the literature are contentious, with different

studies reporting a range of lattice parameters^{22–25} and valence character. 26-29 Some studies also show phase segregation, implying that MCO does not have a stable single phase. 12,30 As will be discussed, these differing results are likely due to variance in the number of Mn³⁺ and Mn⁴⁺ cations in Mn_xCo_{3-x}O₄ samples. Our current work here involves the material characterization of Mn_xCo_{3-x}O₄ films with a wide range of cation stoichiometry from ideal Co₃O₄ to Mn-rich MCO (x = 0 to x = 1.28).

Transition metal spinel oxide materials have the chemical formula AB₂O₄. A-site and B-site cations generally possess a 2+ and 3+ formal charge, respectively. In rare cases, these cations can take on 4+ and 2+ charge states in what are known as "4-2" spinels.³¹ A primary argument in this work is that the ideal singlephase, stoichiometric MCO is a 4-2 spinel with cation valence states of Mn⁴⁺ and Co²⁺ rather than Mn²⁺ and Mn³⁺. Most spinels exhibit a face-centered cubic Bravais lattice structure, although

a)Electronic mail: ryan.comes@auburn.edu

12

some spinels take on tetragonal structures due to the Jahn–Teller (JT) effect. \$4,32-35\$ CMO is well known to possess a tetragonal structure due to the JT effect associated with Mn³+ cations in octahedral coordination. \$1,18-21,32,33,36,37\$ JT distortion does not occur in the case of Mn⁴+ in octahedral coordination, however. In contrast, MCO has been determined to be a cubic spinel by many groups. \$38,39\$ The cubic spinel unit cells can be seen in Fig. 1. Conventional in-plane lattice parameters for spinels with 1st row transition metals range between 8 and 9 Å, \$4\$ but the JT distortion can cause out-of-plane parameters to lie past 9 Å. \$21\$

A normal-type spinel is one in which all A-site cations are tetrahedrally coordinated, and all B-site cations are octahedrally coordinated. CMO is predominately normal-type in which all Co and Mn cations are tetrahedrally and octahedrally coordinated, respectively. 36,37,42,43 The tetragonal structure and high c-parameters of CMO are associated with its normal-type configuration since it puts Mn³⁺ in octahedral coordination, which leads to the JT effect. Co₃O₄ is also known to trend toward a normal-type spinel, with Co²⁺ ions in the A-site and Co³⁺ in the B-site. An inverse-type spinel is one in which all A-site cations and half of the B-site cations are octahedrally coordinated, and half of the B-site cations tetrahedrally coordinated. MCO is predominately inverse-type, 26,45-47 with Co cations split between tetrahedral and octahedral sites. For inverse-type MCO, all Mn cations are octahedrally coordinated just as they are in CMO. This means that the material would be JT-active if Mn is in a 3+ state.

Understanding the MCO of an ideal $MnCo_2O_4$ composition is critical to its future use in energy storage technology, but studying how the material properties change with stoichiometry is also important. This includes how Co- and Mn-rich MCO behaves but also investigating compositions that trend far toward Co_3O_4 and $CoMn_2O_4$. For this reason, $Mn_xCo_{3-x}O_4$ samples with a wide range

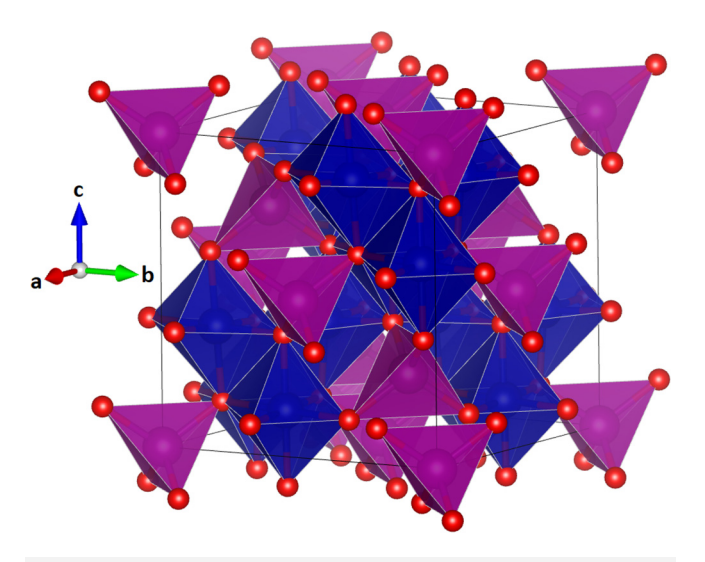


FIG. 1. Conventional unit cell for a cubic structure AB_2O_4 spinel, with purple and blue polyhedral representing A and B cations, respectively. Figure created with VESTA (Ref. 40).

of Co–Mn ratios were grown and studied from ${\rm Co_3O_4}$ to ${\rm CoMn_2O_4}$ with numerous samples in between. Findings from these samples act as a characterization map, showing the material properties as a function of stoichiometry for the entire Co–Mn spinel system. For the purposes of this study, the MCO-region and CMO-region monikers indicate samples whose ${\rm Mn_xCo_{3-x}O_4}$ stoichiometry lies below and above x=1.5, respectively.

II. EXPERIMENT

MCO films were grown on (001)-oriented MAO spinel substrates (a = 8.083 Å, MTI Corporation) using molecular beam epitaxy (MBE). Substrates were sonicated in acetone and isopropyl alcohol for ~5 min each before being loaded into the MBE chamber. Mn and Co metals were deposited concurrently during growth and effusion cells were kept at a constant temperature, with deposition rates calibrated using a quartz-crystal microbalance pregrowth. The sample stage was heated to a constant temperature using an infrared ceramic heating source and measured via a thermocouple on the stage, which causes an overestimation of ~50-100 °C relative to the substrate surface temperature. Samples were grown at 500 °C setpoints and, subsequently, cooled to ambient temperatures over ~30 min. Oxygen gas was introduced into the chamber and maintained at set flow rates during film growth and cooling, which resulted in a slight variation of oxygen pressures between samples, with pressures in the range of $2-3 \times 10^{-5}$ Torr. Significantly lower oxygen pressures are required during cooldown to prevent surface reconstruction of MCO as in CMO. A radiofrequency plasma source at 300 W power was used to significantly increase express expression of atomic O radicals. increase oxygen reactivity via the formation of atomic O radicals.

An *in situ* reflection high-energy electron diffraction (RHEED) system was used to monitor film growth. RHEED was used as sparingly as possible, based on previous observations that the electron beam adversely affects film quality for CMO synthesis. All x-ray photoelectron spectroscopy (XPS) data were collected *in vacuo* using a PHI 5400 system refurbished by RBD Instruments equipped with a monochromator. The system is connected through a vacuum transfer line with the MBE growth chamber, allowing sample surfaces to be measured before exposure to the atmosphere. An electron neutralizer was used during measurements and spectra energy shifted to place O 1s region peaks at 530 eV.

Atomic force microscopy (AFM) topography maps were obtained using a Park XE7 AFM system in the noncontact mode. Rutherford backscattering (RBS) was performed using a 6HDS-2 tandem, National Electrostatics Corporation Pelletron through helium nuclei bombardment. X-ray diffraction (XRD), reciprocal space maps (RSMs), and x-ray reflectivity (XRR) data were gathered using a Rigaku SmartLab diffractometer system with a Cu $K\alpha$ source with a two-bounce Ge(220) monochromator. X-ray absorption spectroscopy (XAS) fluorescence data were collected at the Advanced Photon Source at Sector-20 BM. Both in-plane (parallel) and out-of-plane (perpendicular) polarized spectra were created at both the Co and Mn K-edges.

Cross-sectional scanning transmission electron microscopy (STEM) samples were prepared using an FEI Helios 600 NanoLab DualBeam Ga⁺ focused ion beam (FIB) microscope with a standard

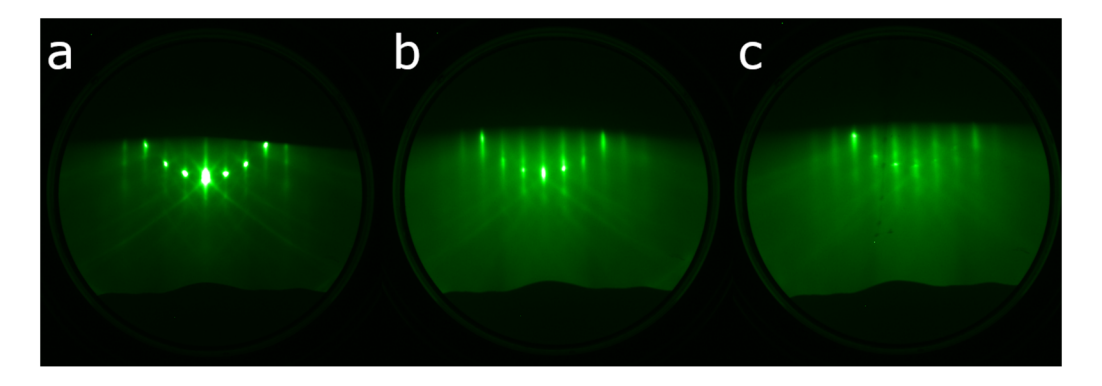


FIG. 2. RHEED patterns for an (a) high-quality surface of Co_3O_4 and $Mn_xCo_{3-x}O_4$ (MCO) films with (b) x = 0.52 and (c) x = 1.02.

lift out procedure. STEM imaging and energy-dispersive x-ray spectroscopy (EDS) mapping were performed on a probe-corrected Thermo Fisher Themis Z microscope operating at 300 kV, with a convergence semi-angle of 25.2 mrad and an approximate collection angle range of 65–200 mrad for high-angle annular dark-field (STEM-HAADF) images.

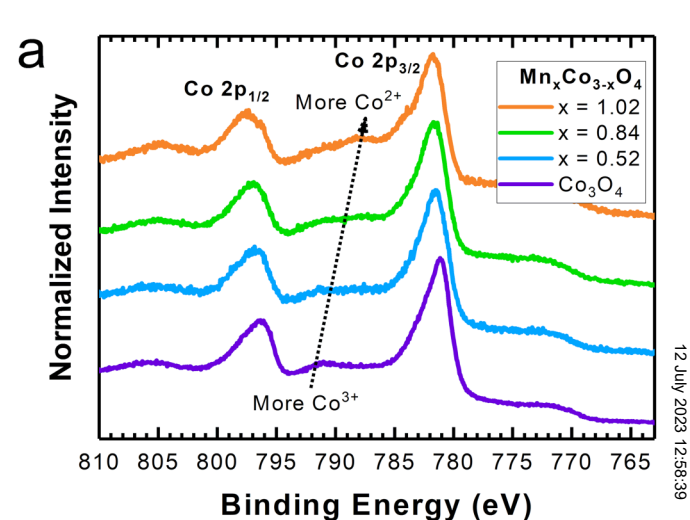
III. RESULTS AND DISCUSSION

A. Film synthesis and initial characterization

RHEED patterns of all samples after cooling revealed them to contain spinel-structure phases, although some patterns show rough or defect-rich surfaces. Example RHEED patterns from key samples discussed in this work are shown in Fig. 2. Figure 2(a) shows a high-quality Co_3O_4 surface, while Figs. 2(b) and 2(c) show x=0.52 and x=1.02 samples. Samples generally showed RHEED patterns with increasing streakiness as x increased and degraded in quality for x greater than 1. As will be seen, these lower-quality RHEED patterns may correlate closely with phase segregation or mixed-valence character of some samples. The stoichiometry of samples was determined by RBS fitting (see supplementary material). Film thickness was determined through fitting of XRR (see supplementary material).

 Co_3O_4 is on the farthest Co-rich end of the Co-Mn spinel system and is a useful starting point for a discussion on MCO's properties as a function of stoichiometry. Co_3O_4 's lattice parameter of 8.086 Å 49 is very close to the MAO substrates' of 8.083 Å leading to a layer-by-layer growth mode with very low lattice strain. High-quality single-crystalline samples of Co_3O_4 were grown and studied using a variety of characterization methods. This confirmed known properties of the ideal material but also provided a baseline for studying how the Co spinel changes with the introduction of Mn. The growth of Co_3O_4 thin films by MBE has been reported in the literature before including synthesis using MAO substrates. 50,51

XPS measurements show a Co 2p spectrum with a satellite feature indicating the mixed 2+ and 3+ character of Co_3O_4 , which comprised 1/3 Co^{2+} and 2/3 Co^{3+} [Fig. 3(a)]. This satellite shape is consistent with other studies involving XPS of Co_3O_4 . In situ XPS of MCO-region samples indicate that all Mn is either in an Mn³⁺ or Mn⁴⁺ state, with no Mn²⁺ found in any sample [Fig. 3(b)]



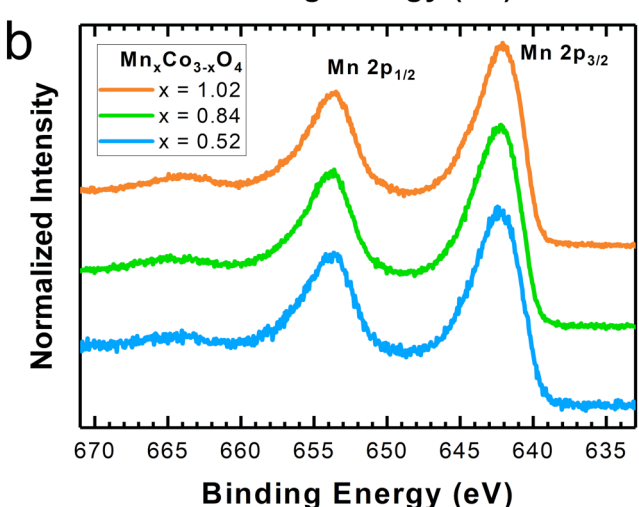


FIG. 3. In situ XPS spectra for (a) Co 2p and (b) Mn 2p core levels for selected samples. Arrow in (a) is a guide to the trend in Co 2p shake-up satellite with valence shift in Co ion.

12 July 2023 12:58:39

discussed in this work. The satellite feature characteristic of Mn²⁺, which would be found between the 2p_{1/2} and 2p_{3/2} peaks, is not seen in Mn 2p spectra. 53,54 Mn 2p spectral shapes of Mn³⁺ and Mn⁴⁺ appear identical, and, thus, even qualitative determination of Mn valence from this region was not attempted. XPS also shows a general trend from mixed Co2+ and Co3+ character toward predominately Co²⁺ character with increasing Mn content. This is seen through the changing shape of the satellite feature of the Co 2p XPS region, which is located between the $2p_{1/2}$ and $2p_{3/2}$ peaks [Fig. 3(b)]. The changes show progressively less indication of Co³⁺ in higher-Mn samples, with some samples even depicting ideal Co² satellite features. 21 These results suggest that the addition of Mn to Co₃O₄ yields charge transfer from Mn to Co, which would be likely to produce a Mn⁴⁺ and Co²⁺ formal charge. However, the ambiguity of the Mn charge state from XPS and the surface sensitivity of the technique makes it difficult to decouple any surface segregation or valence instabilities in the near-surface region from bulk properties. Additional analysis using XAS will be presented below to further elucidate trends in the valence with the Mn content.

X-ray diffraction of the film is consistent with a cubic FCC spinel structure, and the OOP (004) peak is convolved with the substrate indicating the small lattice mismatch between the film and substrate [Fig. 4(b)]. RSMs showed that single-phase samples were coherently strained to the substrate, as shown in Fig. 4(c) for x = 1.02. The alignment of the (206) peaks along the Q_x axis for the MAO substrate and (206) MCO film streak in Fig. 4(c) indicates that they share the same in-plane lattice constant. Extracted out-of-plane lattice constants for the cubic spinel phase are shown in Fig. 5, with selected samples color-coded to match their data in other figures. Starting with the characterization results of Co_3O_4 helps in discussing changes in material properties that come with the introduction of Mn into the spinel system towards $MnCo_2O_4$. MCO-region (x < 1.5) samples tended to exhibit phase segregation behavior with increasing Mn content.

Phase segregation presented itself most clearly in OOP XRD data in which secondary film peak signals were apparent in some samples. Location, intensity, and broadness of the peaks varied greatly among phase segregated samples, with some examples being shown in Fig. 4(a). It is not clear if all peaks are due to the (004) spinel diffraction condition or if some reflect a material with a different crystal structure, such as rocksalt MnO or CoO, which would exhibit diffraction peaks between 39° and 42°. However, there was no evidence of the Mn²⁺ charge state from XPS analysis for any sample, which would suggest that the rocksalt phase is not the predominant phase in the system. Peaks at values of 2θ between 37° and 39° are consistent with tetragonal Co_{1-v}Mn_{2+v}O₄ films that undergo the JT distortion from a cubic spinel. Selected samples, including x = 0.93, x = 1.28, and x = 0.46 [denoted by an * in Fig. 4(b)] show diffraction intensity consistent with a tetragonal phase. As will be shown later from XAS analysis, even samples that appear to be single-phase in XRD, such as x = 1.02 and x = 1.10, show a tendency to display mixed Mn valence characters between Mn³⁺ and Mn⁴⁺ and may have localized tetragonal distortions. Such behavior is likely to reduce stability within the material and promote the phase segregation that we have observed in some samples by XRD.

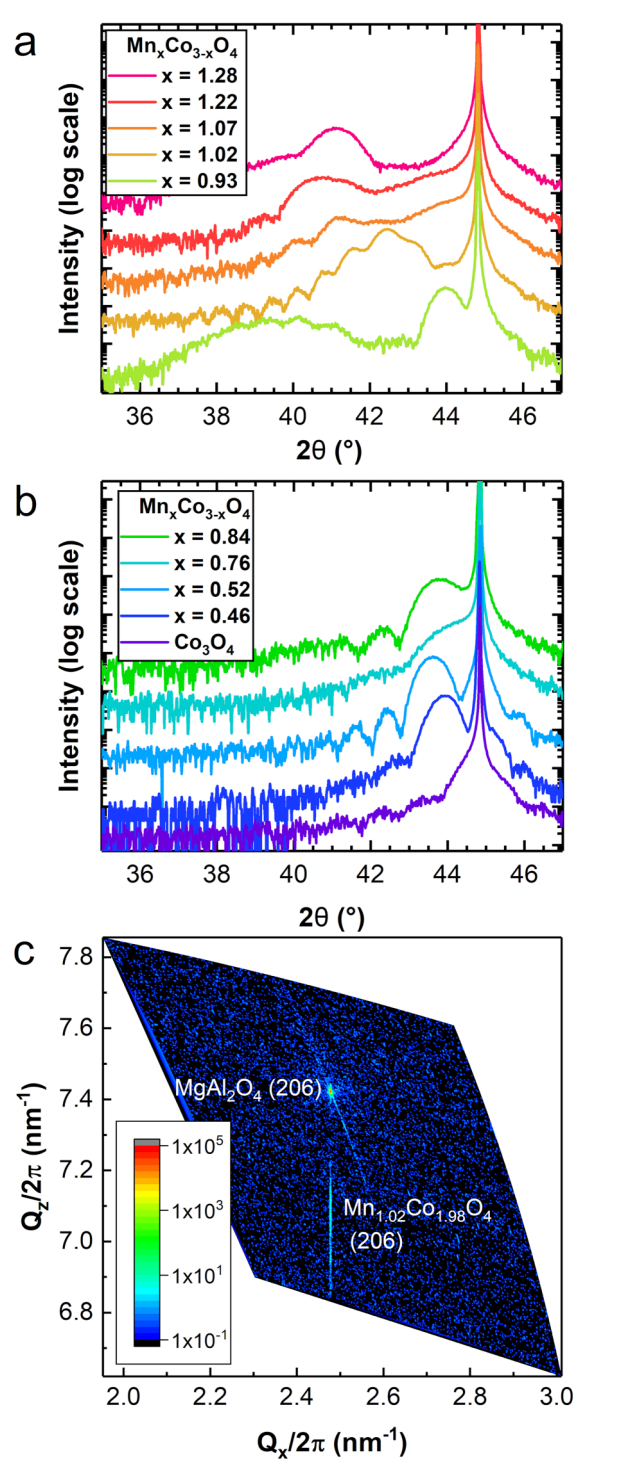


FIG. 4. Out-of-plane XRD spectra of MCO-region samples (a) and (b) for varying x values about the (004) spinel film peaks. Larger x values (a) generally show multiple peaks. (c) Reciprocal space map of x = 1.02 sample about (206) peak. * in (b) indicates the tetragonal secondary phase.

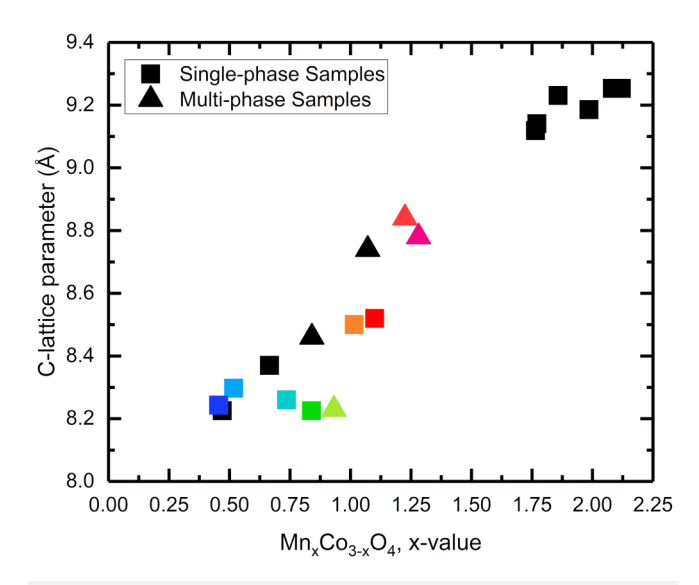


FIG. 5. Out-of-plane lattice parameters for Co-Mn spinel samples as a function of Mn concentration. Lattice parameters for x < 1.5 are extracted from the cubic spinel peak and do not account for other phases that may be present. Tetragonal spinel samples from Ref. 21 are included for comparison for x > 1.75. Samples included in other figures are color-coded to other legends. Single-phase samples are shown as squares and multiphase as triangles.

Three possible contributions can be given to the rising cparameter. (1) Mn ions generally exhibit a larger ionic radius than Co ions with the same valence state,⁵⁵ leading to longer bond lengths and unit cells. (2) Ionic radii of cations and thus bond lengths change depending on their valence state and coordination environment. Samples with octahedral Mn with valence character trending toward Mn3+ (1.96 or 2.025 Å) rather than Mn4+ (1.91 Å) will show greater lattice constants.⁵⁵ (3) JT distortion of Mn³⁺ octahedra causes immense stretching along the out-of-plane lattice direction as seen in CMO.²¹ As will be shown later through multiple analyses, Mn cations appear to occupy octahedral coordination sites in MCO-region samples. Greater Mn content means a higher percentage of Mn3+ octahedra in samples with mixed-valence character. Previous studies of ideal stoichiometry MnCo2O4 show a reported cubic structure with a lattice parameter of 8.09 to 8.29 Å, $^{22-24}$ but the sample in this study closest to ideal MCO (x = 1.02) shows an out-of-plane lattice parameter of 8.50(1) Å, suggesting some degree of JT activity despite the apparent single phase based on XRD.

B. Electron microscopy

To further probe phase segregation in the samples, STEM and EDS measurements were performed on samples x = 0.76 and x = 1.02. These results are shown in Figs. 6 and 7, respectively. STEM-HAADF images [Fig. 6(a)], in which contrast is proportional to atomic number $Z^{-1.7}$, confirm the overall uniformity of the x = 0.76 film, while STEM bright-field (BF) [Fig. 6(b)] images show no significant strain or other line defects, such as phase separation or misfit dislocations. Fast Fourier-transform (FFT) maps of the substrate and film confirmed the results from RSM data, indicating that the films are coherently strained to the substrate (see supplementary material).65 STEM-EDS compositional analysis [Fig. 6(c)] for x = 0.76 also confirms a homogeneous sample with a uniform structure and no evidence of Co and Mn segregation in the regions examined.

In contrast, the STEM-EDS map for x = 1.02 [Fig. 7(c)] shows that Co and Mn are distributed heterogeneously within the film, 8 with some Mn cations having migrated toward the sample surface. However, no clear secondary phases are observed, with the exception of a surface reconstruction in the top few unit cells, which can likely be attributed to atmospheric exposure, as indicated by

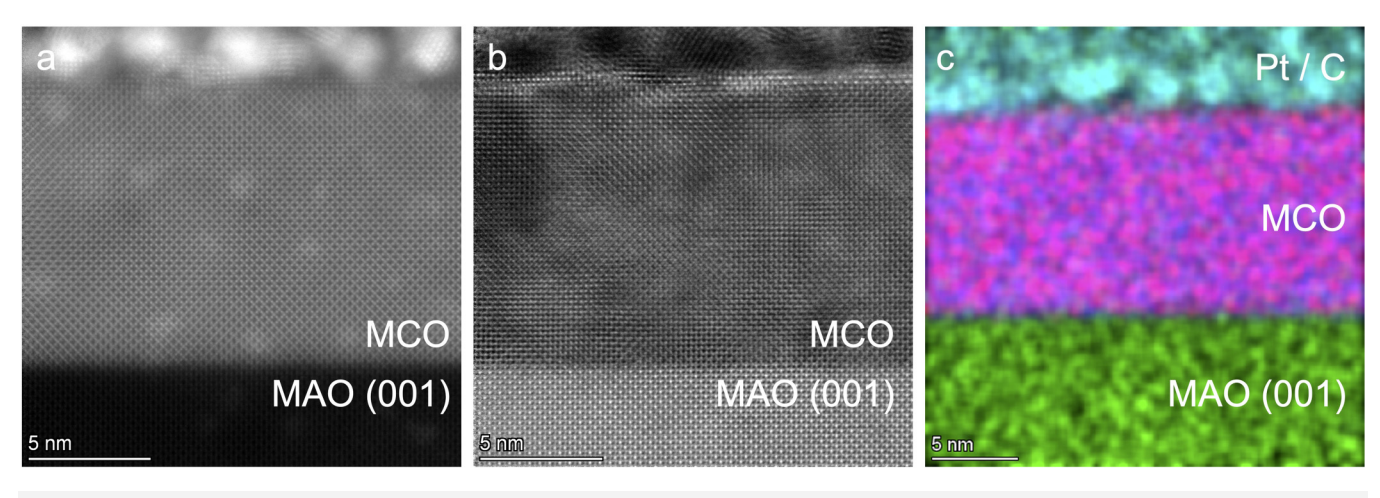


FIG. 6. Scanning transmission electron microscopy images of the x = 0.76 sample. (a) Drift-corrected STEM-HAADF image; (b) BF image; (c) composite STEM-EDS map of the sample showing Co K (blue), Mn K (red), Mg K (green), and Pt L (cyan) peaks. The mottled contrast in the HAADF is from Pt redeposition during TEM preparation. Images were taken along the MAO [100] zone-axis. Bright spots in (a) are due to redeposition of the Pt capping layer during FIB lift out.

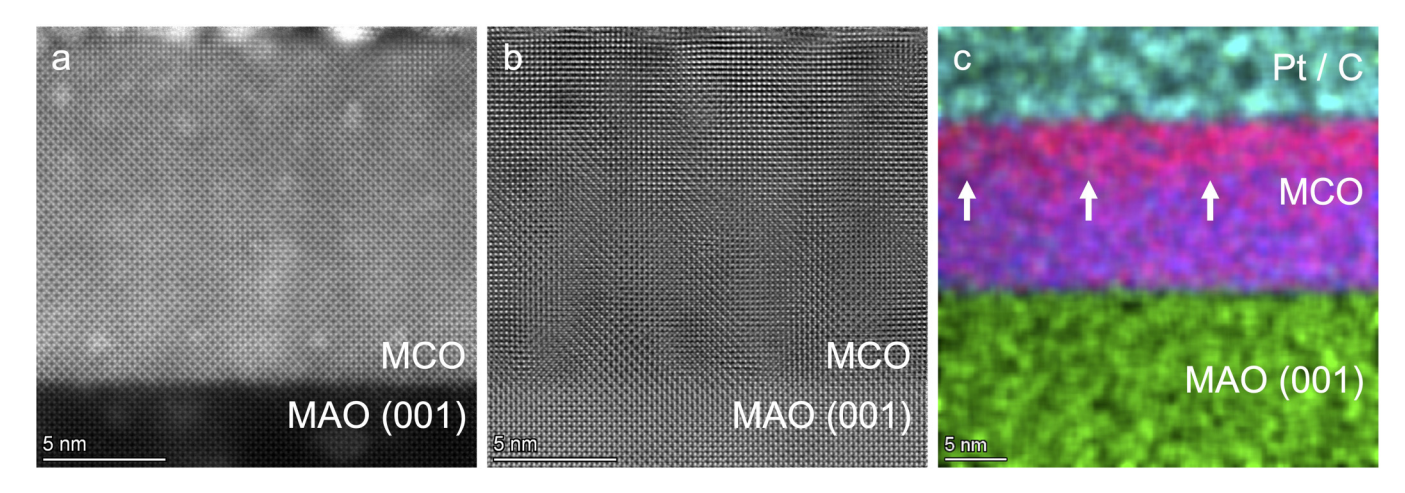


FIG. 7. Scanning transmission electron microscopy images of x = 1.02 sample. (a) Drift-corrected STEM-HAADF image; (b) BF image; (c) composite EDS map of the sample showing Co K (blue), Mn K (green), and Pt L (cyan) peaks. The arrows in (c) mark the relative increase in the Mn content near the film surface. The mottled contrast in the HAADF is from Pt redeposition during TEM preparation. Images were taken along the MAO [100] zone-axis. Bright spots in (a) are due to redeposition of the Pt capping layer during FIB lift out.

STEM-HAADF and STEM-BF images [Figs. 7(a) and 7(b)]. The cation segregation in this sample that has close-to-ideal MnCo₂O₄ stoichiometry leads to the question of whether a stable single-phase version of the material exists, or whether it will seek to form multiple phases as seen in samples of other studies. 12,30 Diffusion of Mn adatoms toward the surface may be attributable to low oxygen chemical potential and oxygen vacancies, producing JT-active Mn³ cations that would preferentially move toward the film surface rather than occupy lattice sites in the cubic spinel.

C. X-ray absorption spectroscopy

XAS was performed on Co₃O₄ along with other MCO-region samples over a range of film stoichiometries. Incident x rays were linearly polarized, allowing for the acquisition of data sensitive to either the in-plane or out-of-plane lattice directions only. A large pre-edge peak is seen in the spectra of both polarizations near the Co K-edge in Fig. 8(a), indicating tetrahedral coordination of Co cations in the sample. As will be seen, this pre-edge peak appears in Co XANES spectra for all MCO-region samples, indicating that tetrahedral sites remain occupied by Co and additional Mn occupies octahedral sites. This is also consistent with the presumed inverse-type spinel structure of MCO.

As was the case in CMO, analysis of the EXAFS region allowed for determination of cation-nearest oxygen bond lengths in Co₃O₄ and other MCO-region samples (see supplementary material).65 However, Co cations are both tetrahedrally and octahedrally coordinated, which means that spectra contain information from both lengths and fitting must account for both contributions. This can be done by introducing scattering paths for both octahedral and tetrahedral coordination into the fits and adjusting the weighting values in the fits to account for the multiple sites.

One possible combination of lengths for tetrahedral Co²⁺ and octahedral Co³⁺, respectively, is 1.91(1) and 1.90(1) Å from the

in-plane spectrum and 1.92(1) and 1.91(1) Å from the out-of-plane spectrum. Despite the fact that these values for tetrahedrally coordinated Co²⁺ are lower than the value of 1.96 Å predicted through theoretical crystal radii,55 fitting error was low (see supplementary material)⁶⁵ and similar bond lengths have been reported in other EXAFS analyses of Co₃O₄. ^{57,58} Crystal strain is unrelated to this shrinking in tetrahedral bond length since the lattice mismatch between the substrate and film is minor. As will be seen, similar bond lengths were determined for other Co spectra of MCO-region samples, indicating that values did not vary greatly with the addition of Mn.

Assuming additional Mn takes on octahedral coordination as indicated in multiple analyses of this study, this lowering of Co valence could correspond with charge transfer from Mn to Co. In this case, Mn⁴⁺ occupation of octahedral sites would produce a corresponding Co²⁺ for charge balancing, thereby leading to idealized MnCo₂O₄ valences of Mn⁴⁺ and Co²⁺. As will be shown, many of the MCO-region samples of this study show mixed-valence characters between Mn³⁺ and Mn⁴⁺. This indicates that both octahedral site substitutions may take place, with JT-active Mn3+ leading to higher c-lattice parameters. The increase in phase segregation with higher Mn concentrations appears closely tied to the increasing lattice parameter and increase in JT-active Mn³⁺, which is unstable in the cubic spinel lattice.

In-plane and out-of-plane polarized XAS was performed on MCO-region samples with a range of stoichiometry from Co₃O₄ to Mn-rich MCO. Out-of-plane Mn spectra show significant variation with changing stoichiometry through the appearance of a pre-edge feature at ~6550 eV of the K-edge, which is denoted by an arrow in Fig. 8(e). This pre-edge feature intensity is similar in appearance to the pre-edge features shown in out-of-plane Mn spectra of epitaxial tetragonal CMO samples.²¹ This indicates that changing properties between samples, including phase segregation tendency and multivalence character, are driven by Mn but not Co. It is important to

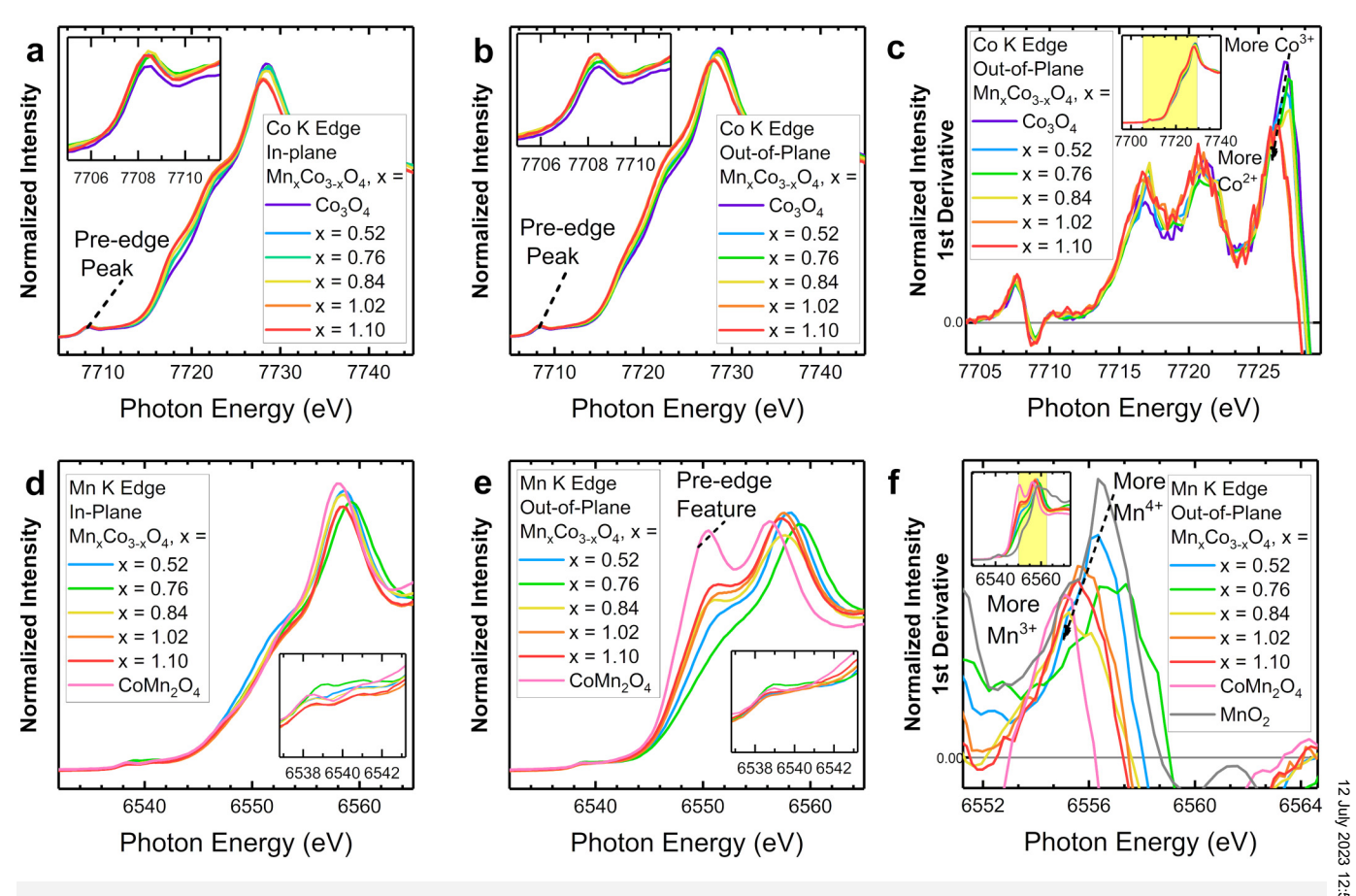


FIG. 8. Co K-edge XANES data for (a) in-plane and (b) out-of-plane polarizations with insets showing magnified pre-edge peaks, and (c) 1st derivative of out-of-plane data. Mn K-edge XANES data for (d) in-plane and (e) out-of-plane polarizations with magnified insets showing the absence of pre-edge peaks and (f) 1st derivative of out-of-plane data. CoMn₂O₄ reference data are adapted from Ref. 21.

note that this large pre-edge feature at \sim 6550 eV is distinct from the pre-edge peaks at \sim 6538 eV that are commonly associated with tetrahedral coordination of Mn⁵⁹ and which we observe in the Co K-edge data in the insets of Figs. 8(a) and 8(b). The insets in Figs. 8(d) and 8(e) show the absence of such a feature and absorption features that are consistent with sixfold coordinated Mn from the literature⁵⁹ and from our previous work on CoMn₂O₄ (Ref. 21). Our polarization-dependent results also suggest that the changing material properties are rooted in causes that are anisotropic along the out-of-plane direction, such as the Jahn–Teller distortion.

Mn³⁺ character most likely explains the appearance of the pre-edge feature. Based on in-plane polarization measurements, most of these MCO-region samples exhibit some mixed Mn valence character between 3+ and 4+, while reference CMO samples comprised solely Mn³⁺. Considering the relatively large c-lattice parameters of these MCO-region samples and the tetragonal crystal structure of CMO, this pre-edge feature may be a general indication of JT distortion of Mn³⁺ octahedra and of a tetragonal crystal structure. Also, the existence of these pre-edge features further supports the idea that all Mn cations in

MCO-region samples take on octahedral coordination. One $Mn_xCo_{3-x}O_4$ sample, x=0.76, shows no pre-edge feature intensity in its out-of-plane Mn spectrum, indicating that this sample is comprised predominately of Mn^{4+} . While this single-phase, single-valence sample is Co-rich compared to $MnCo_2O_4$ stoichiometry, it may be an indication that ideal MCO does have a stable single phase with Mn^{4+} and Co^{2+} valence states.

Co-region XANES for all samples and both polarizations show high-intensity pre-edge peaks at the base of the K-edge [insets of Figs. 8(a) and 8(b)]. The intensities of the peaks are consistent between samples and, because pre-edge intensity is an indication of tetrahedral coordination for Co, ⁵⁹ all tetrahedral sites appear to be fully occupied by Co, regardless of sample stoichiometry. This follows for an inverse-type MCO spinel in which all Co would be found in tetrahedral sites and further supports the idea that Mn takes on octahedral coordination.

Analysis of Co-region XAS first derivative plots for both polarizations also shows trends in Co valence from mixed 2+ and 3 + toward Co²⁺ with increasing Mn stoichiometry. These results are highlighted in Fig. 8(c) with an arrow indicating the trend in Co



valence. Linear combination fitting of both in-plane and out-of-plane Co-region spectra shows a trend in valence character from mixed Co2+ and Co3+ toward Co2+ with increasing Mn stoichiometry (see Table S2 in the supplementary material). Fitting was performed by using Co₃O₄ (2.67+ Co valence) and CMO (2+ Co valence) spectra as fitting standards and agrees with the 1st derivative analysis. While these results are in agreement, we prefer to focus on trends rather than attempt to quantify the Co formal valence based on the linear combination fitting. The trend in Co valence confirms what was also seen in comparing Co 2p XPS spectra discussed above in Fig. 3(a).

Likewise, linear combination fitting of in-plane Mn shows no clear trend with varying stoichiometry and indicates the mixedvalence character of the MCO-region samples of this study that is consistent with differing degrees of phase segregation between samples. Fitting was performed using CMO (3+ Mn valence) and MnO₂ (4+ Mn valence) as standards and results confirm that most samples exhibit mixed Mn3+ and Mn4+ character. While linear combination fitting can show general trends in cation valences between samples, exact valence determination is not possible since fitted and reference spectra do not share identical structures. Instead, we again employ the 1st derivative of the Mn out-of-plane data to show the trend in valence across samples, as shown in Fig. 8(f), with an arrow demonstrating the trend direction with increasing x value.

MCO-region samples show cations with multiple coordinations and mixed-valence characters, making EXAFS fitting a challenge. Not only do theoretical ionic radii depend on cation coordination and valence state,⁵⁵ but also JT distortion drives large changes in bond lengths with the introduction of Mn³⁺ in octahedral sites. This is especially problematic in fitting out-of-plane Mn spectra for samples that show both Mn3+ and Mn4+. All this leads to multiple bond lengths in the material for a given cation and must be accounted for in fitting spectra by introducing additional scattering paths into the fitting algorithm. Determining multiple bond lengths from one spectrum is difficult when the contribution of each length in a sample is not known.

The x = 0.76 sample does not show multiple bond lengths in its out-of-plane Mn spectrum and can be fit in a straightforward manner, as seen in Fig. 9. This sample shows in-plane and out-of-plane Mn-O bond lengths in octahedral coordination of 1.90 Å and 1.91 Å, respectively, both of which correspond closely to reported bond lengths for Mn^{4+,55} The slightly smaller in-plane bond length would be expected from the compressive epitaxial strain. This indicates, as other analyses of this study do, that this single-phase sample exhibits primarily Mn⁴⁺ character and no Mn³⁺. While its stoichiometry is Co-rich, this MCO-region sample shows no mixed-valence character and may exemplify the closest to the chemical ideal of MnCo₂O₄, namely, an Mn valence state of 4+.

All analyses suggest that Mn in the MCO-region samples of this study are octahedrally coordinated but also show mixed Mn valence character between Mn3+ and Mn4+. While other studies of MCO report mixed-valence character as well, 26-29 an ideal spinel should generally show single-valence states for each cation meaning that mixed-valence character is a reflection of defects in the material. OOP XRD c-lattice parameters steadily increase with the addition of Mn indicating the action of JT-distorted Mn³⁺ octahedra

due to oxygen vacancies in the films. Co K-edge XANES pre-edge peaks show consistent high intensity indicating that tetrahedral sites are occupied by Co cations leaving Mn to occupy octahedra. The appearance of a pre-edge feature in out-of-plane Mn-region XANES spectra indicates JT-active Mn³⁺ octahedra in MCO-region samples since CMO also shows this feature and contains only Mn³⁺ octahedra. Transformed EXAFS spectra for out-of-plane Mn spectra show multiple nearest-neighbor oxygen bond lengths, which most likely comes from the simultaneous occupation of octahedral sites with both Mn3+ and Mn4+ cations. This octahedral coordination of Mn also confirms the inverse-type spinel nature of MCO and stoichiometry-varied samples from Co₃O₄ to Mn-rich MCO. While Mn3+ may not be the ideal Mn valence for singlephase MCO, the fact that samples show this character allows the octahedral coordination of Mn to be observed in this study, primarily through the act of JT distortion.

D. Discussion

There have been numerous studies of MCO in the nanocrystalline form, 1,4,12,19,60,61 but very few studies involving thin film samples 46,62 and none reporting the growth of MCO using molecular beam epitaxy (MBE). However, studies involving experimental characterization have shown mixed results in the literature. Some studies report single-phase samples and others report phase segregation and mixed-valence composition 12,26-30 These include studies reporting Mn⁴⁺ character^{26–29} and others showing only Mn³⁺. This suggests that it is challenging to synthesize high-quality single-phase MCO or that a single-crystalline version of MCO may be metastable.

While 2+ and 3+ are the cation valences of most spinels, $\frac{\omega}{12}$ single-crystalline, fully oxidized MCO appears to exhibit Mn⁴⁺ and $\frac{\omega}{12}$ Co²⁺ states. In the case of standard Mn²⁺ and Co³⁺, inverse-type MCO would place Co³⁺ into tetrahedral coordination, which is rarely observed. This is due to the unfavorable configuration of unpaired e_g orbitals associated with Co³⁺ in tetrahedral coordination. 63 This leads to the notion that Co may instead take on a much more favorable 2+ valence with Mn oxidizing to a 4+ state for charge balance. Other studies of MCO showing Mn⁴⁺ character support this idea, 26-29 however, without single-phase samples and reliable characterization, it has been difficult to confirm.

Our study has sought to characterize high-quality MBE-grown MCO films to determine cation valences and investigate the propensity for phase segregation. Our results show that phase stability is highly dependent on oxygen stoichiometry, which is limited to low 10⁻⁵ Torr (with plasma active) in MBE. Further optimization of growth rate and sample temperature could be pursued to determine if alternative conditions lead to a more stable window for MCO growth.

From the findings of this study, it is clear that the MnCo₂O₄ phase stability is highly dependent on processing conditions and prone to phase segregation due to a miscibility gap between Co₃O₄ and CoMn₂O₄ type phases. The sample closest to this stoichiometry is the $Mn_xCo_{3-x}O_4$ sample x = 1.02, which shows evidence of cation segregation in STEM and mixed-valence character between Mn^{3+} and Mn^{4+} based on XANES. Samples with x ~ 1.2 had clear



phase segregation based on XRD, and selected additional samples with lower x also were spontaneously phase segregated.

A key sample in this study from the single-phase MCO-region is the x=0.76 sample, which shows solely Mn^{4+} character. In this sample, out-of-plane polarization Mn K-edge XANES shows no indication of a pre-edge feature associated with Mn^{3+} . EXAFS fitting shows near-identical Mn–O bond lengths for both in-plane and out-of-plane polarization spectra, the values of which correspond closely to Mn^{4+} octahedra. The first derivative XAS also suggests the sample shows predominately Mn^{4+} character. As discussed in the supplementary material, 65 the x=0.76 sample was grown at the high

end of the oxygen pressure range for this study ($\sim 3 \times 10^{-5}$ Torr), which may explain the greater concentration of Mn⁴⁺.

OOP XRD also shows that the c-lattice parameter of sample x=0.76 is lower than those of other MCO-region samples. Lower lattice parameters have been reported previously for ideal MCO²²⁻²⁴ with values trending as low as 8.09 Å. This suggests that the sample x=0.76 is closer in lattice parameter to true, single-phase MCO than the other MCO-region samples of this study which show greater lattice parameters. It was discussed earlier how these other MCO-region samples show higher c-lattice parameters due to the effects of JT distortion and

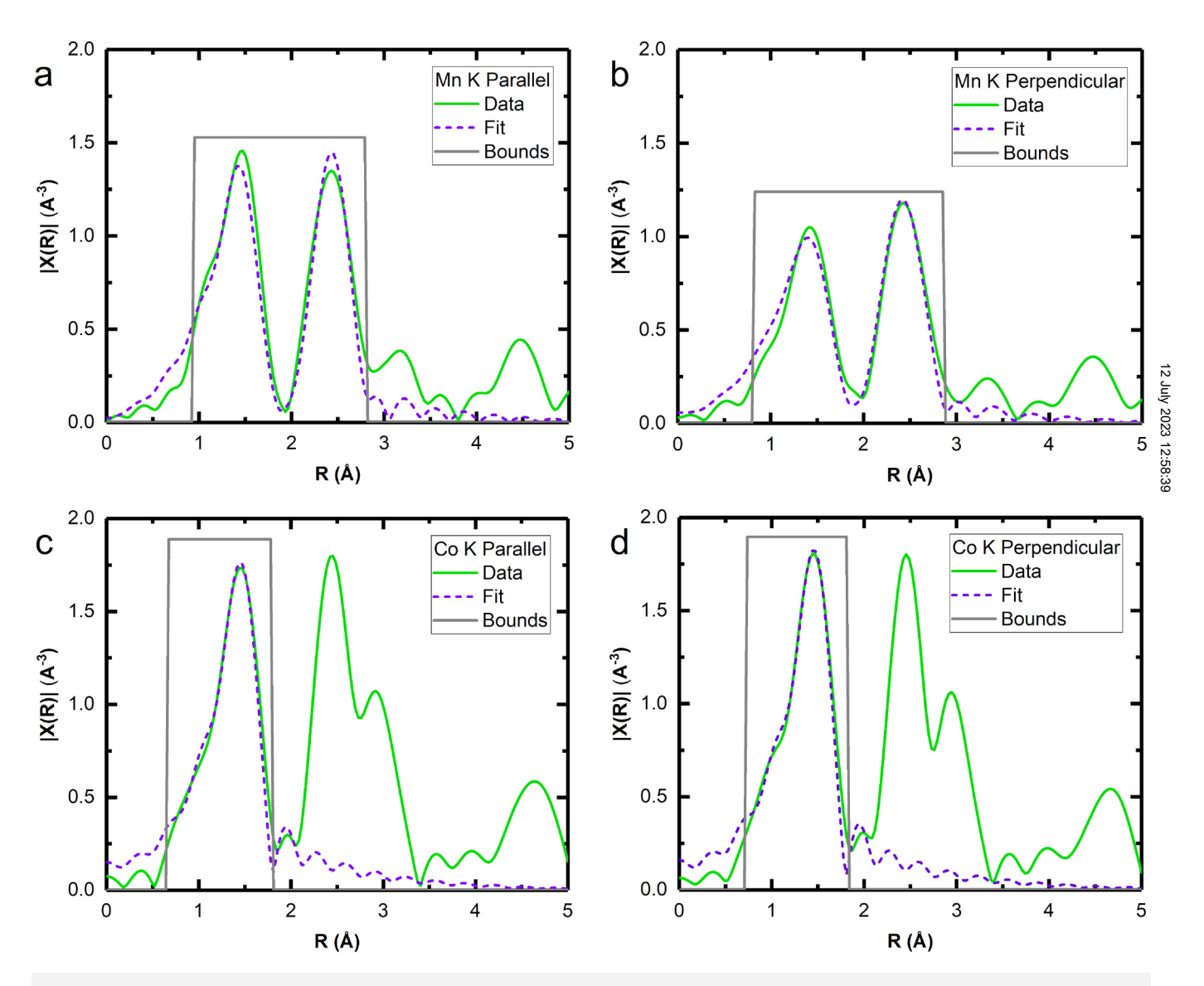


FIG. 9. Fits to EXAFS data for x = 0.76 sample for Mn K-edge with (a) parallel (in-plane) polarization, (b) perpendicular (out-of-plane) polarization, and Co K-edge (c) and (d) with the same polarization.

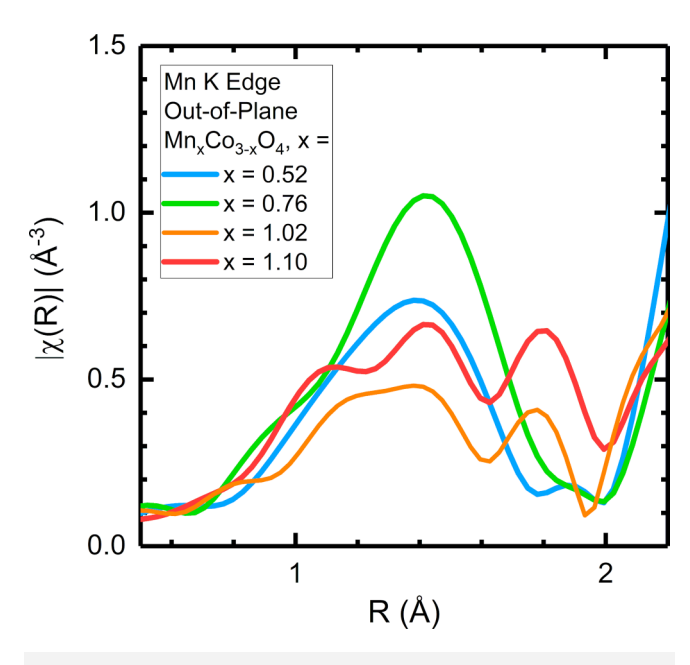


FIG. 10. Mn K-edge EXAFS data for out-of-plane polarization for selected stoichiometries

polyhedral stretching of octahedral Mn3+. Thus, Mn4+ seems to be the characteristic valence of ideal MCO, while Mn³⁺ represents valence state defects. These defects then act to drive the material into larger lattice parameters through JT distortion and promote phase segregation if the crystal must accommodate Mn3+ and Mn⁴⁺ characters in the same phase.

While sample x = 0.76 is Co-rich, its single-phase, singlevalence and smaller lattice parameter suggests that ideal MnCo₂O₄ does have a stable single-crystalline phase with an Mn valence of Mn⁴⁺. Additionally, XPS and XAS show a trend in Co valence from mixed 2+ and 3+ towards Co2+ with increased Mn stoichiometry for MCO-region samples, indicating that charge transfer from Mn to Co on the octahedral sites occurs. This would mean that studies showing mixed-valence character or phase segregation involve should be viewed with this in mind.

A transition from ideal MnCo₂O₄ (Mn⁴⁺ and Co²⁺) towards CoMn₂O₄ (Co²⁺ and Mn³⁺) via the addition of Mn would see the substitution of Mn3+ cations into the spinel structure. While MCO possesses a cubic crystal structure with non-JT-active Mn⁴⁺ octahedra, CMO exhibits a tetragonal structure due to its distorted Mn³⁺ octahedra. Due to the incompatibility between cubic and tetragonal c-lattice parameters, the transition in stoichiometry from MCO towards CMO and replacement of Mn4+ with Mn3+ in octahedral sites produces stoichiometries that likely do not have a stable single phase. Instead, the coexistence of Mn^{4+} and Mn^{3+} may lead to regions of the cubic and tetragonal structure that would favor phase segregation over a homogenous structure due to a miscibility gap in the Mn-Co spinel phase diagram. This is supported by our observation of multiple phases in XRD at higher x values, including diffraction intensity in the tetragonal regime, as shown in Fig. 3(a). It is also

supported by the appearance of multiple bond lengths from EXAFS data in Fig. 10 for x = 1.02 and 1.10 and the larger XANES pre-edge feature for the Mn K-edge perpendicular polarization in Fig. 8(e).

Limited work has been reported on the Co-Mn spinel phase diagram, but Golikov et al. have previously observed such a miscibility gap in bulk ceramics.⁶⁴ Their work reported that the phase diagram is highly dependent on the preparation and thermal treatment process, which is consistent with our observations. The thin films that we have synthesized here are also qualitatively consistent with observations by Yang et al. of phase segregation in Co-Mn spinel nanoparticles, where they observed formation of a nearly stoichiometric Co₃O₄ core and Mn₃O₄ shell. We suggest that there is still a large parameter space to explore in this rich phase diagram for these technologically relevant materials.

IV. CONCLUSIONS

This study is the first to synthesize and study MCO-region samples using MBE, and one of the only studies of MCO oriented toward thin films. The samples studied include ideal stoichiometry $MnCo_2O_4$ and $Mn_xCo_{3-x}O_4$ ranging from x = 0 to 1.28. The samples show increasing c-lattice parameters and phase segregation tendencies with additional Mn contents. Co valence trends toward Co2+ from mixed 2+ and 3+ with increasing Mn. While most samples suggest mixed Mn valence between 3+ and 4+, the Mn³⁺ character likely originates from oxygen deficiency, with Mn4+ being the proper formal valence in fully oxidized MnCo₂O₄. This means the single-phase valence states of stoichiometric MnCo₂O₄ are likely Mn⁴⁺ and Co²⁺. Mn³⁺ character in MCO-region samples is likely due to insufficient $\frac{1}{N}$ oxygen reactivity during growth, which is more prominent in samples $\underline{\underline{\xi}}$ with greater Mn concentrations. Oxygen-deficiency in MCO leads to the JT distortion of Mn³⁺ octahedra and promotes phase segregation and formation of rocksalt (Mn,Co)O and tetragonal $Co_xMn_{3-x}O_4$ $\overset{7}{b}_{60}$ phases. It is this JT distortion of Mn^{3+} octahedra that contributes to the large increases in c-lattice parameters of MCO-region samples.

ACKNOWLEDGMENTS

M.D.B. gratefully acknowledges support from the Alabama EPSCOR Graduate Research Scholars Program. M.D.B. and R.B.C. gratefully acknowledge support from the National Science Foundation (NSF) through Award No. NSF-DMR-1809847. X-ray diffraction measurements were performed on a system supported by the NSF Major Research Instrumentation (MRI) program under award number 2018794. B.E.M. and S.R.S. were supported by the Chemical Dynamics Initiative/Investment under the Laboratory Directed Research and Development (LDRD) Program at Pacific Northwest National Laboratory (PNNL). PNNL is a multiprogram national laboratory operated for the U.S. Department of Energy (DOE) by Battelle Memorial Institute under Contract No. DE-AC05-76RL01830. A portion of this research was performed at the W. R. Wiley Environmental Molecular Sciences Laboratory, a DOE User Facility sponsored by the Office of Biological and Environmental Research and located at PNNL. This research used resources from the Advanced Photon Source, an Office of Science User Facility operated for the U.S. Department of Energy (DOE) Office of Science by Argonne National Laboratory and was supported by the U.S. DOE under Contract No. DE-AC02-06CH11357.



AUTHOR DECLARATIONS

Conflict of Interest

The authors have no conflicts to disclose.

Author Contributions

Miles D. Blanchet: Conceptualization (equal); Formal analysis (lead); Investigation (lead); Methodology (lead); Writing - original draft (lead); Writing - review & editing (supporting). Bethany E. Matthews: Formal analysis (supporting); Investigation (supporting); Visualization (supporting); Writing - review & editing (supporting). Steven R. Spurgeon: Formal analysis (supporting); Investigation (supporting); Visualization (supporting); Writing review & editing (supporting). Steve M. Heald: Formal analysis (supporting); Investigation (supporting); Writing - review & editing (supporting). Tamara Isaacs-Smith: Formal analysis (supporting); Investigation (supporting); Writing - review & editing (supporting). Ryan B. Comes: Conceptualization (equal); Funding acquisition (lead); Methodology (supporting); Project administration (lead); Resources (lead); Supervision (lead); Writing - original draft (supporting); Writing – review & editing (lead).

DATA AVAILABILITY

The data that support the findings of this study are available within the article and its supplementary material. Additional data that support the findings of this study are available from the corresponding author upon request.

REFERENCES

- ¹F. Cheng, J. Shen, B. Peng, Y. Pan, Z. Tao, and J. Chen, Nat. Chem. 3, 79 (2011).
- ²Y. Li and J. Lu, ACS Energy Lett. 2, 1370 (2017).
- ³E. Antolini, ACS Catal. 4, 1426 (2014).
- ⁴C. Li, X. Han, F. Cheng, Y. Hu, C. Chen, and J. Chen, Nat. Commun. 6, 7345 (2015). ⁵P. G. Bruce, S. A. Freunberger, L. J. Hardwick, and J.-M. Tarascon, Nat. Mater.
- 11, 19 (2011). ⁶L. Malavasi, C. A. J. Fisher, and M. S. Islam, Chem. Soc. Rev. 39, 4370 (2010).
- ⁷K. Kinoshita, Electrochemical Oxygen Technology (Wiley, New York, 1992).
- ⁸M. K. Debe, Nature **486**, 43 (2012).
- ⁹B. C. H. Steele and A. Heinzel, Nature **414**, 345 (2001).
- ¹⁰H. N. Cong, K. E. Abbassi, and P. Chartier, J. Electrochem. Soc. **149**, A525 (2002).
- ¹¹E. Rios, J.-L. Gautier, G. Poillerat, and P. Chartier, Electrochim. Acta 44, 1491 (1998).
- 12Y. Yang, Y. Xiong, M. E. Holtz, X. Feng, R. Zeng, G. Chen, F. J. DiSalvo, D. A. Muller, and H. D. Abruña, Proc. Natl. Acad. Sci. U.S.A. 116, 24425 (2019). 13Y. Liang, H. Wang, J. Zhou, Y. Li, J. Wang, T. Regier, and H. Dai, J. Am. Chem. Soc. 134, 3517 (2012).
- ¹⁴D. S. McClure, J. Phys. Chem. Solids 3, 311 (1957).
- 15 H. Zhu, S. Zhang, Y.-X. Huang, L. Wu, and S. Sun, Nano Lett. 13, 2947 (2013).
- ¹⁶Z. Li, K. Gao, G. Han, R. Wang, H. Li, X. S. Zhao, and P. Guo, New J. Chem. **39**, 361 (2014).
- 17 L. Hu, H. Zhong, X. Zheng, Y. Huang, P. Zhang, and Q. Chen, Sci. Rep. 2, 986
- ¹⁸L. Zhou, D. Zhao, and X. W. Lou, Adv. Mater. **24**, 745 (2012).
- 19 J. Li, S. Xiong, X. Li, and Y. Qian, Nanoscale 5, 2045 (2013).
- ²⁰M. H. Kim, Y. J. Hong, and Y. C. Kang, RSC Adv. 3, 13110 (2013).
- ²¹M. D. Blanchet et al., J. Phys.: Condens. Mat. 33, 124002 (2021).
- 22Y. Mouhib, M. Belaiche, S. Briche, C. A. Ferdi, and E. Iffer, Mater. Res. Express 6, 035508 (2018).

- ²³S. Yuvaraj, A. Vignesh, S. Shanmugam, and R. Kalai Selvan, Int. J. Hydrogen Energ. 41, 15199 (2016).
- ²⁴S. G. Krishnan, M. H. A. Rahim, and R. Jose, J. Alloy. Compd. **656**, 707 (2016).
- 25 B. Saravanakumar, G. Ravi, V. Ganesh, R. K. Guduru, and R. Yuvakkumar, Mater. Sci. Energy Technol. 2, 130 (2019).
- ²⁶N. Garg, M. Mishra, X. Govind, and A. K. Ganguli, RSC Adv. 5, 84988 (2015).
- ²⁷L. Zou, J. Cheng, Y. Jiang, Y. Gong, B. Chi, J. Pu, and L. Jian, RSC Adv. 6, 31248 (2016).
- ²⁸G. Mitran, S. Chen, and D.-K. Seo, RSC Adv. 10, 25125 (2020).
- ²⁹B. L. Ahuja, A. Dashora, N. L. Heda, S. Tiwari, N. E. Rajeevan, M. Itou, Y. Sakurai, and R. Kumar, Appl. Phys. Lett. 97, 212502 (2010).
- 30Y. Yang, R. Zeng, Y. Xiong, F. J. DiSalvo, and H. D. Abruña, Chem. Mater. 31,
- 31 C. Biagioni and M. Pasero, Am. Mineral. 99, 1254 (2014).
- 32 J. B. Goodenough, A. Wold, R. J. Arnott, and N. Menyuk, Phys. Rev. 124, 373 (1961).
- 33 J. B. Goodenough and A. L. Loeb, Phys. Rev. 98, 391 (1955).
- ³⁴D. P. Shoemaker, J. Li, and R. Seshadri, J. Am. Chem. Soc. 131, 11450 (2009).
- 35 L. E. Orgel and J. D. Dunitz, Nature 179, 462 (1957).
- 36B. Boucher, R. Buhl, and M. Perrin, J. Appl. Phys. 39, 632 (1968).
- 37D. Das, R. Biswas, and S. Ghosh, J. Phys.: Condens. Matt. 28, 446001 (2016).
- **38**T. Nguyen, M. Boudard, L. Rapenne, O. Chaix-Pluchery, M. J. Carmezim, and M. F. Montemor, RSC Adv. 5, 27844 (2015).
- 39 M. M. S. Sanad, A. K. Yousef, M. M. Rashad, A. H. Naggar, and A. Y. El-Sayed, Phys. B 579, 411889 (2020).
- 40 K. Momma and F. Izumi, J. Appl. Crystallogr. 44, 1272 (2011).
- ⁴¹M. G. Brik, A. Suchocki, and A. Kamińska, Inorg. Chem. **53**, 5088 (2014).
- 42 C. D. Spencer and D. Schroeer, Phys. Rev. B 9, 3658 (1974).
- ⁴³A. D. Pelton, H. Schmalzried, and J. Sticher, Ber. Bunsen-Ges. Phys. Chem. 83, 241 (1979).
- 44L. Suchow, J. Chem. Educ. 53, 560 (1976).
- 45 S. Singh, P. Pramanik, S. Sangaraju, A. Mallick, L. Giebeler, and S. Thota, J. Appl. Phys. 121, 194303 (2017). J. Appl. Phys. 121, 194303 (2017).
- 46K. J. Kim and J. W. Heo, J. Korean Phys. Soc. 60, 1376 (2012).
 47S. Liu, D. Ni, H.-F. Li, K. N. Hui, C.-Y. Ouyang, and S. C. Jun, J. Mater.
 Chem. A 6, 10674 (2018).
 48S. Thapa, R. Paudel, M. D. Blanchet, P. T. Gemperline, and R. B. Comes, &
- J. Mater. Res. 36, 26 (2021).
- 49 C. A. F. Vaz, V. E. Henrich, C. H. Ahn, and E. I. Altman, J. Cryst. Growth 311, 2648 (2009).
- 50 K. J. Kormondy et al., J. Appl. Phys. 115, 243708 (2014).
- 51 C. A. F. Vaz, D. Prabhakaran, E. I. Altman, and V. E. Henrich, Phys. Rev. B 80, 155457 (2009).

 52 K. M. Cole, D. W. Kirk, and S. J. Thorpe, Surf. Sci. Spect. 28, 014001 (2021).
- ⁵³S. Matzen et al., Phys. Rev. B 83, 184402 (2011).
- 54 A. R. C. Bredar, M. D. Blanchet, A. R. Burton, B. E. Matthews, S. R. Spurgeon, R. B. Comes, and B. H. Farnum, ACS Catal. 12, 3577 (2022).
- 55R. D. Shannon, Acta Cryst. A 32, 751 (1976).
- ⁵⁶J. Yano and V. K. Yachandra, Photosynth. Res. **102**, 241 (2009).
- 57L. Bai, M. Pravica, Y. Zhao, C. Park, Y. Meng, S. V. Sinogeikin, and G. Shen, J. Phys.: Condens. Matter 24, 435401 (2012).
- 58 A. Bashir et al., Nanoscale 10, 2341 (2018).
- **59**T. Yamamoto, X-Ray Spectrom. **37**, 572 (2008).
- 60 T. Oh, S. Ryu, H. Oh, and J. Kim, Dalton Trans. 48, 945 (2019).
- ⁶¹D. S. Baji, H. S. Jadhav, S. V. Nair, and A. K. Rai, J. Solid State Chem. 262, 191 (2018).
- 62K. Uusi-Esko, E.-L. Rautama, M. Laitinen, T. Sajavaara, and M. Karppinen, Chem. Mater. 22, 6297 (2010).
- 63D. L. Wood and J. P. Remeika, J. Chem. Phys. 46, 3595 (1967).
- 64Yu. V. Golikov, S. Ya. Tubin, V. P. Barkhatov, and V. F. Balakirev, J. Phys. Chem. Solids 46, 539 (1985).
- 65See supplementary material online for details on atomic force microscopy, growth conditions, x-ray diffraction, and EXAFS analysis.